PAPER

Check for updates

Photothermal properties of a nanofluid containing graphene oxide-copper nanoparticle hybrid materials prepared by using *Paramignya trimera* extract

Nguyen Van Hao, [iD] [a] Nguyen Thi Ngoc Mai,[a] Mone Phommahaxay,[a] Vu Xuan Hoa,[a] Pham The Tan,[b] Do Tuan,[c] Pham Van Nhat,[d] Bui Hung Thang,[c] Phan Ngoc Minh[d] and Pham Van Trinh [iD] *[cd]

This study reports the green synthesis, characterization, and photothermal performance of graphene oxide–copper nanoparticle (GO–CuNP) hybrid nanofluids. The hybrid materials were fabricated using graphene oxide (GO) as a template and *Paramignya trimera* (*P. trimera*) extract as a reducing and stabilizing agent, producing uniformly distributed Cu nanoparticles (∼8.5 nm) on GO sheets. The prepared nanofluids (0.01–0.04 vol%) exhibited enhanced thermal conductivity and optical absorption compared with deionized water. The thermal conductivity increased by 4–15% in the temperature range 30–55 °C. Zeta potential analysis revealed values of 38.5, 32.6, 30.8, and 26.2 mV, indicating good colloidal stability up to 0.03 vol% and moderate stability with incipient aggregation at 0.04 vol%. Under AM 1.5 solar irradiation, the GO–CuNP nanofluids demonstrated photothermal conversion efficiencies of 35–62%, which are higher than those of nanofluids containing GO and CuNPs only. This was attributed to synergistic plasmonic–graphenic absorption and improved heat transport within the hybrid structure. These findings highlight the potential of hybrid nanofluids as efficient solar-absorbing media for solar thermal applications.

1. Introductions

Because of their unique properties, hybrid nanofluids have become interesting candidates with enormous potential applications. These innovative fluids, which are produced by dispersing several nanostructures and additional additives in a base fluid, have remarkable thermal, electrical, and optical characteristics that make them appealing to numerous sectors.[1] Graphene (Gr) and graphene oxide (GO) based nanofluids are attractive candidates for future cooling and solar energy absorption systems owing to their superior thermal conductivity.[2–5] The incorporation of Gr and its derivatives into nanofluids is well suited for direct-absorption solar collectors (DASCs), where the working fluid itself functions as the optical absorber, eliminating thermal resistance between the absorber and the collector.[6] Early studies by Zhang *et al.*[7] and Vakili *et al.*[8]

demonstrated that graphene-based nanofluids exhibit superior thermal conductivity and photothermal conversion efficiency compared with other carbon nanomaterial suspensions, with both properties increasing as nanoparticle concentration rises. Khosrojerdi *et al.*[9] further reported that GO nanoplatelet nanofluids achieve an absorption efficiency of up to 99.6% at a concentration of 0.045 wt%. Subsequent work by Chen *et al.* expanded on the thermophysical behavior and stability of GO/water systems.[10] Unfortunately, graphene tends to aggregate together to form graphene clusters in base fluids due to π–π stacking. The development of hybrid materials of graphene and other nanomaterials including metal-based nanostructures could solve the above remaining problems.[11–15] In hybrid nanofluids, Campos *et al.* showed that GO–Ag hybrid structures can significantly enhance photothermal performance, achieving thermal efficiencies up to 75%.[16] Zeng *et al.* examined how particle morphology affects the solar-thermal conversion and sensible heat storage of TiO₂@GO binary nanofluids.[14] Their results indicated that, at low concentrations, both nanosphere- and nanosheet-structured TiO₂@GO provide superior sensible heat conversion performance.[14] Copper (Cu) nanoparticles, on the other hand, exhibit excellent intrinsic thermal conductivity and plasmonic absorption in the visible region, making them highly suitable for solar-thermal applications.[17,18]

[a]Institute of Sciences and Technology, TNU – University of Sciences, Tan Thinh Ward, Thai Nguyen City, Vietnam

[b]Hung Yen University of Technology and Education, Khoai Chau Distr., Hung Yen Province, Vietnam

[c]Institute of Materials Science, Vietnam Academy of Science and Technology, 18 Hoang Quoc Viet Str., Cau Giay Distr., Hanoi, Vietnam. E-mail: trinhpv@ims.vast.vn

[d]Graduate University of Science and Technology, Vietnam Academy of Science and Technology, 18 Hoang Quoc Viet Str., Cau Giay Distr., Hanoi, Vietnam

When combined into a GO–Cu hybrid system, the carbon–metal interaction improves electron–phonon coupling, suppresses oxidation of Cu, and enhances the stability and heat transfer capability of the nanofluids.[19–21] Shaik et al. investigated the thermophysical properties of Cu-graphene hybrid nanofluid and found that the nanofluids exhibit a remarkable thermal conductivity enhancement of approximately 35% even at very low hybrid nanoparticle concentrations.[22] Trinh et al., reported an enhancement of 41% in the thermal conductivity with nanofluids containing graphene-carbon nanotube/Cu hybrid materials.[23] The reported studies on the nanofluids containing graphene-Cu hybrid materials were mainly focused on the thermal conductivity. However, the photothermal properties of graphene-Cu nanofluids has not been investigated and reported so far. In solar energy conversion systems, such hybrid nanofluids can enhance performance through several mechanisms: (i) stronger broadband solar absorption due to the coexistence of plasmonic Cu and wide-band absorption of GO, (ii) increased thermal conductivity facilitating faster heat transport, (iii) micro-convection generated by Brownian-driven nanoparticle motion, and (iv) reduced interfacial thermal resistance at the solid–liquid boundary.[24,25] These synergistic properties make GO–Cu hybrid nanofluids promising candidates for next-generation solar collectors, photothermal devices, and direct absorption solar systems. Up to now, various techniques exist for fabricating graphene–Cu hybrid nanomaterials, many conventional synthesis routes rely on toxic chemicals or complex, energy-intensive procedures. Recent progress in green synthesis has demonstrated that plant extracts—rich in flavonoids, polyphenols, terpenoids, and alkaloids—can effectively reduce and stabilize metal nanoparticles.[26] The plant-mediated methods offer simplicity, low toxicity, and biocompatible products, while bioactive compounds also help prevent nanoparticle agglomeration.[26] Paramignya trimera extract has recently been applied to the synthesis of AgNPs and corresponding nanofluids, underscoring the potential of natural materials for producing non-oxide nanostructures.[27] Such green approaches are essential for developing hybrid nanofluids with improved thermophysical properties.

The objective of this study is to synthesize the nanofluid incorporating GO–CuNP hybrid materials by a green method utilizing P. trimera extract as a reducing agent. The morphological and structure of GO–CuNP hybrid materials as well as the photothermal properties of nanofluid containing GO–CuNP hybrid materials were investigated and presented.

2. Experimental

2.1. Materials

Graphite powder (purity > 99%, Sigma-Aldrich) with an average particle size of 5 μm, copper(II) sulfate (CuSO₄, analytical grade, Merck), sodium hydroxide (NaOH, 99.5%, Xilong Chemical), and all other reagents were used as received. Paramignya trimera plants collected in Phu Quoc Island (Vietnam) were used to prepare the P. trimera extract.

2.2. Preparation of nanofluids

The preparation process of nanofluid containing GO–CuNP hybrid materials is presented in Fig. 1. Firstly, GO was synthesized by using the Hummers' method.[28] The obtained GO (Fig. S4-SI) was dispersed in DI water with a concentration of 1 g L^{-1} by using ultrasonication technique. Typically, 50 mL of 1 mM CuSO₄ solution was mixed with 10 mL of GO suspension (1 mg mL^{-1}) under magnetic stirring for 6 h at a temperature of 20 °C. After that, 10 mL of the P. trimera extract obtained from P. trimera roots as reported in the previous study[27] was added dropwise to the mixture under constantly stirring for 12 hours at room temperature. Afterwards, the obtained solution was centrifuged at 10 000 rpm for 10 min and repeated 3 times to separate the GO–Cu hybrid materials from the mixture. The prepared GO–CuNP hybrid material was washed three times with water and ethanol, then dispersed in DI water by using bath ultrasonication for 45 min (40 kHz, 150 W, Elmasonic S 30 H) to create the nanofluids with concentrations of 0.01 vol%, 0.02 vol%, 0.03 vol% và 0.04 vol%. The nanofluids containing GO and CuNPs with a concentration of 0.01 vol% were also prepared (SI) to compare the photothermal properties.

2.3. Characterization

The morphology, particle size, and elemental composition of the synthesized materials were analyzed using Field Emission Scanning Electron Microscopy and Energy Dispersive X-ray Spectroscopy (EDS) with a Hitachi S4800 FESEM and Transmittance Electron Microscopy (TEM, JEOL 2100). XRD patterns of samples were measured by using a Brucker D8 Endeavor with the radiation source of Cu-K$_\alpha$ at $\lambda = 1.54056$ Å. The optical absorption characteristics of materials were measured using a UV-vis spectrometer (Jassco-V770, Japan) within the wavelength range of 250 to 800 nm. Fourier transform infrared (FTIR) spectroscopy was employed to examine the chemical compositions using a PerkinElmer Fourier transform infrared spectrometer (Spectrum Two, USA) in a range of 500–2500 cm^{-1}, with a resolution 4 cm^{-1}. Raman spectra of samples were acquired using a Horiba XploRA ONE Raman spectrometer with laser excitation at 532 nm. The stability of prepared nanofluids was evaluated by using Horiba SZ-100. Thermogravimetric measurements of the synthesized samples were carried out using a Shimadzu DTG-60H TG/DTA instrument (Japan). The analyses were conducted under an air atmosphere with a gas flow rate of 30 mL min^{-1} and a heating rate of 10 °C min^{-1}. The specific surface areas (S_{BET}) of the samples were evaluated by nitrogen adsorption–desorption isotherms at 77 K using a Micromeritics TriStar 3000 V6.07A system (USA). The thermal conductivity of the nanofluids was assessed in a range of temperature from 30 °C to 55 °C using an HTL-04 (Eternal Engineering Equipment Ltd, India) with an uncertainty of ±2.0%. The detail of the calibration of the thermal conductivity measurement of the prepared nanofluids was presented in the SI. The photothermal properties of nanofluid was measured by a designed system as illustrated in Fig. 2. It comprised a solar light source AM 1.5G irradiation (1000 W m^{-2}), a thermocouple, and a data collector. The data collector recorded the
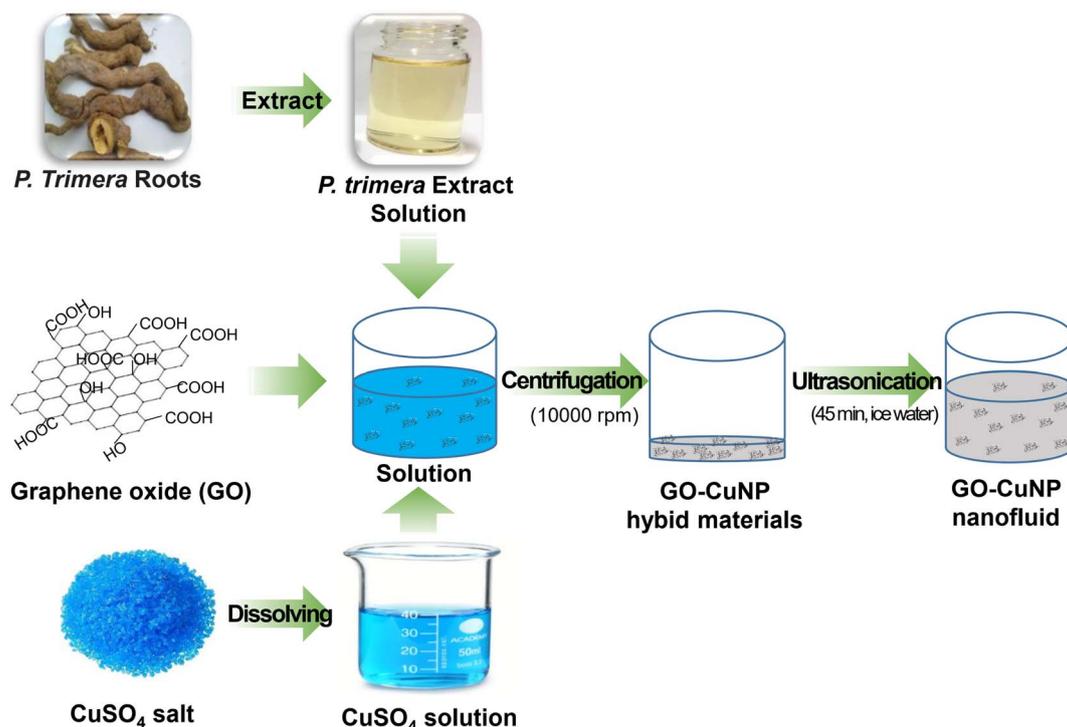
Fig. 1 Preparation process of nanofluid containing GO–CuNP hybrid materials using *P. trimera* extract as reducing agent.

temperature of the nanofluids every 300 seconds for a total duration of 3600 seconds. The reported values of thermal conductivity and photothermal conversion efficiency are an average of five measurements of each sample.

3. Results and discussions

3.1. GO–CuNP hybrid materials

Fig. 3a is the SEM image of the GO–CuNP hybrid material after fabrication. The average CuNPs size was determined to be about 8.5 nm (Fig. 3b). The CuNPs were tightly attached to the surface of the GO sheets. This can be explained by the fact that when the material was fabricated, the solution used for synthesis already contained GO. On the surface of GO, there are functional groups such as –COOH, –OH, these functional groups will act as centers

to capture Cu^{2+} ions dispersed in the solution and thus prevent these ions from clumping together to form large particles.[29,30] Zhao *et al.* showed that Cu^{2+} ions can be effectively adsorbed onto GO through interactions with carboxyl and hydroxyl functional groups.[31] Fig. 3c presents the HRTEM image of the GO–Cu hybrid material, revealing that the Cu nanoparticles are uniformly distributed across the GO surface. Measurement of the lattice spacing of the nanoparticles shows a value of approximately 0.209 nm, which corresponds to the (111) plane of metallic Cu. This structural identification is further supported by the TEM–EDS analysis provided in Fig. 3d.

Fig. 4 displays the SEM-EDS analysis of GO–Cu hybrid materials, indicating the percentage composition and the strongest elemental peak specific to carbon (C). Copper (Cu)
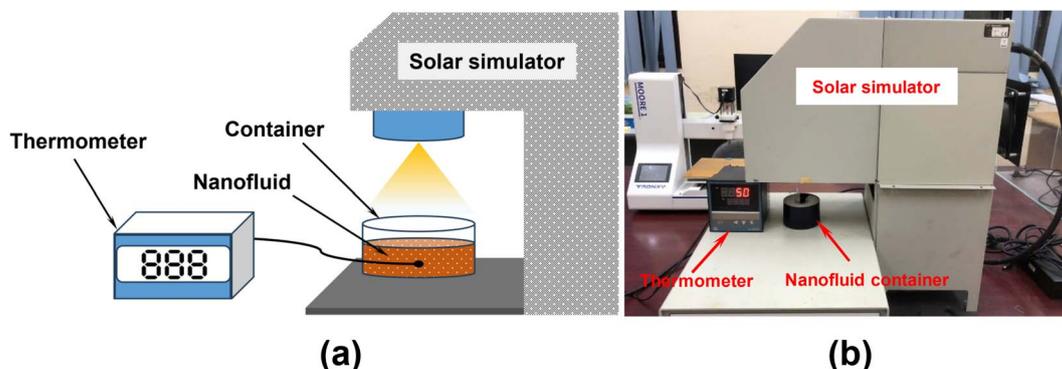

Fig. 2 (a) Schematic diagram and (b) actual photograph of photothermal conversion system of nanofluids containing GO–CuNP hybrid materials.
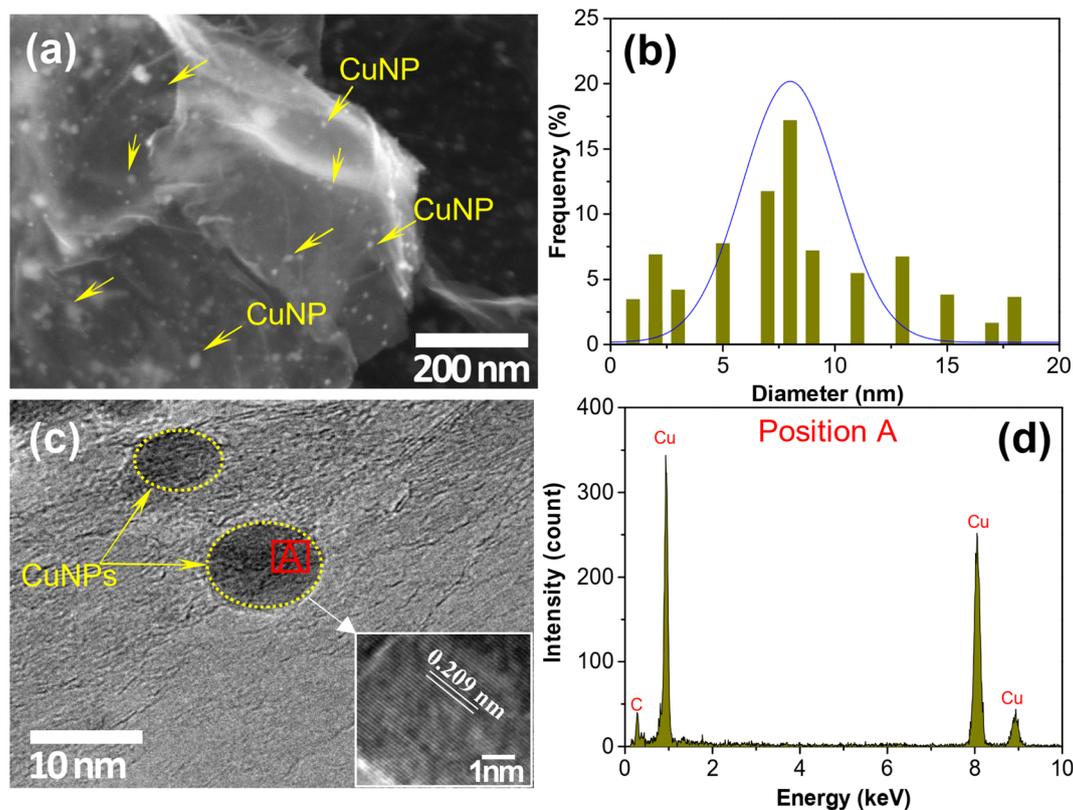
Fig. 3 (a) SEM image, (b) size distribution of CuNPs, (c) TEM image and (d) TEM-EDS of GO–CuNP hybrid material.

metal and oxygen (O) additionally presented through a few more minor peaks. The relative quantities of C, O and Cu. As a result, the Cu content is around 1.32%. The presence of Cu and O elements was confirmed by the element mapping. The obtained results indicated the effective deposition of CuNP onto the GO. This is in a good agreement with the SEM image (Fig. 3a) which shows a uniform distribution of CuNPs on the surface of GO.
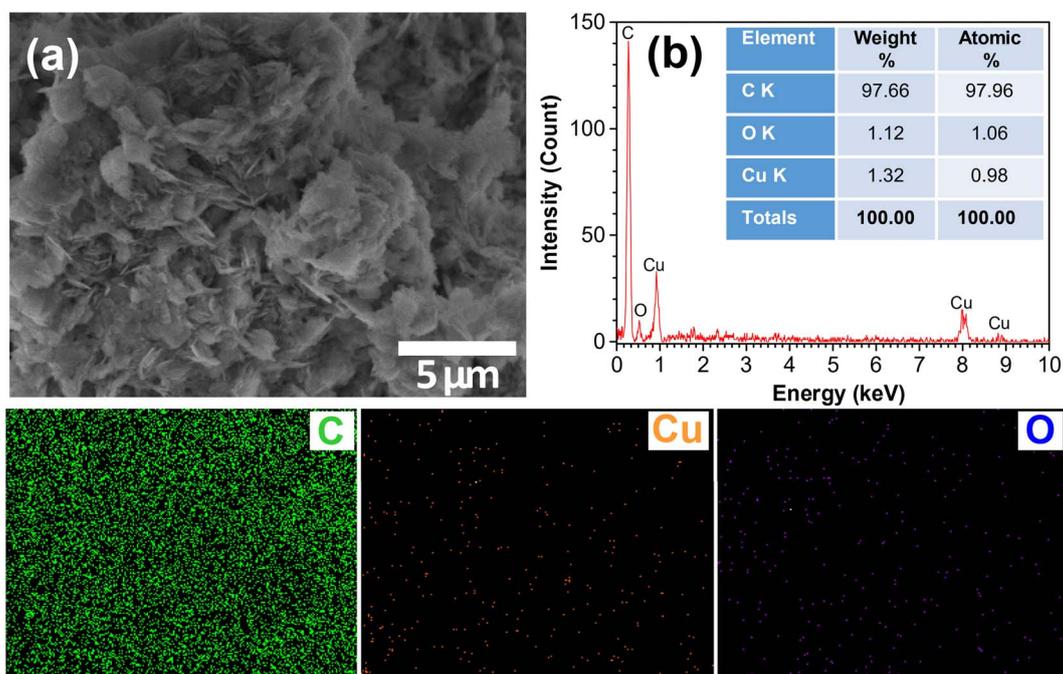

Fig. 4 SEM-EDS analysis of GO–Cu hybrid materials (a) SEM images, (b) EDS spectra and element mapping.

Fig. 5a presents the X-ray diffraction (XRD) patterns of GO and GO–CuNP hybrid materials. The diffraction pattern of GO exhibits peaks at $2\theta = 10.1°$ and $26.2°$ corresponding to the (001) and (002), respectively. In the case of GO–CuNP hybrid materials, some peaks are observed at $43.2°$ and $50.4°$ which are indexed to the (111) and (200) planes of Cu. The average crystallite size of Cu domains was calculated based on the (111) reflection at $2\theta = 43.2°$ by using the Scherrer eqn (1):[32]

$$D = \frac{0.9\lambda}{\beta \cos \theta} \tag{1}$$

The calculated crystallite size is $\sim$10.7 nm, consistent with SEM and TEM results as discussed in the previous section. The existence of oxide phases such as CuO, Cu_2O was not observed in the XRD pattern, which may be due to the relatively low content. These results, supported by both XRD and morphological studies, confirm the formation of well-dispersed, highly crystalline CuNPs on the surfaces of GO.

Fig. 5b shows the UV-vis spectrum of GO and GO–CuNP hybrid material. As can be seen, only a typical peak at 226 nm was detected for GO. This implied that the presence of GO dispersed in water. As for GO–CuNP hybrid nanofluids displays two surface plasmon resonance peaks at 260 nm and 529 nm corresponding to GO and CuNPs, respectively. This demonstrated that the GO–CuNP hybrid materials were successfully synthesized in water. Fig. 5c shows the FTIR spectrum of the *P. trimera* extract, GO and GO–CuNPs hybrid materials. FTIR peaks for *P. trimera* extract, GO and GO–CuNPs hybrid materials are presented in Table 1. The results showed that the absorption bands at 1639, 1451, 1381, 1034 and 656 cm^{-1} for the *P. trimera* extract. This implied that the extract contains some functional groups such as carbonyl, amine and phenols, *etc.*[33] The FTIR spectra of GO revealed the presence of oxygen-containing species, indicating functional groups on the surface of GO sheets. Prominent peaks were seen at 1639, 1382, and 1055 cm^{-1}, corresponding to the stretching vibrations of C=O bonds in carbonyl and carboxylic groups. This confirmed that the functional groups were attached to the surface of GO. For GO–CuNP hybrid material, it is interesting noted that the presence of a typical peak around 523 cm^{-1}. This characteristic peak is attributed to the formation of Cu–O stretching vibrations.[34-36] This implied the presence of the interactions between Cu^{2+} and the functional groups in the extract. As a result, FTIR analysis indicates that the phytochemicals in *P. trimera* extract including phenols and flavonoids, facilitate the reduction and stabilization of Cu^{2+} ions to produce CuNPs. The GO and GO–CuNP hybrid materials were further characterized using Raman spectroscopy. The synthesized GO and GO–CuNP hybrid material exhibited two distinct absorption bands at around 1580 cm^{-1} and 1330 cm^{-1}, corresponding to G and D bands, respectively. The G band represents the bond stretching of sp^2 hybridization of C. The D band corresponds to the breathing mode of aromatic rings with dangling bond in-plane terminations. The Raman spectra of GO and GO–CuNP are presented in Fig. 5d. As can be seen, the I_D/I_G ratios of GO and GO–CuNP were determined to be 0.73 and 1.03, respectively.

The increase of the I_D/I_G ratio in GO–CuNP hybrid materials may be attributed to the presence of functional groups and the defects introduced by CuNPs decorated on the surface.

Fig. 5e shows the N_2 adsorption–desorption isotherms of GO and GO–CuNP at 77 K. As observed, the adsorption and desorption behaviors of GO and GO–CuNP differ noticeably. When evaluating specific parameters such as the BET specific surface area (S_{BET}), the GO–CuNP hybrid exhibits a higher surface area of 189.02 m^2 g^{-1} compared to pristine GO (160.11 m^2 g^{-1}). This indicates that the incorporation of CuNPs increases the specific surface area of the hybrid material relative to GO. This result is in good agreement with the surface morphological observations discussed in the preceding section. Fig. 5f presents the TGA curves of GO and GO–CuNPs. The results show that pristine GO undergoes thermal decomposition in an air atmosphere, exhibiting three distinct weight-loss stages. The first weight-loss stage, occurring from 25 to 100 °C, is attributed to the removal of physically adsorbed moisture. Other significant weight-loss stages appear in the ranges of 130–350 °C and 380–520 °C. The initial peak around 170 °C is ascribed to the elimination of oxygen-containing functional groups from the GO surface, while the sharp peak near 400 °C is associated with the combustion of the carbon framework of the graphene sheets. TGA measurements were employed to estimate the mass fraction of CuNPs in the GO–CuNP hybrid material. The TGA curve of GO–CuNP exhibits similar characteristic stages to those of GO, corresponding to moisture evaporation, decomposition of oxygen-containing functional groups on the GO surface, and carbon degradation. Complete carbon decomposition is observed at approximately 500 °C. The residual mass after thermal treatment is about 2.5%, which is attributed to the remaining CuNP-derived products after carbon combustion. This value is higher than that obtained from EDS analysis, which may be due to the transformation of Cu into copper oxide species such as Cu_2O or CuO during the combustion process.

3.2. Formation mechanism of GO–CuNP hybrid material

Fig. 6 shows the Cu^{2+} ionic reduction mechanism on Cu^0 on the GO sheets using *P. trimera* extract. The formation mechanism of the GO–CuNP hybrid material using *Paramignya trimera* (*P. trimera*) extract as a reducing agent involves a series of chemical and physical interactions, which can be delineated as follows:

Initially, graphene oxide (GO) was synthesized *via* the Hummers' method and dispersed in DI water at a concentration of 1 g L^{-1} using ultrasonication. The GO sheets are characterized by oxygen-containing functional groups, such as carboxyl (–COOH) and hydroxyl (–OH), which are distributed across their surface, as confirmed by FTIR analysis (Fig. 5c). These functional groups serve as active sites for the coordination of Cu^{2+} ions.[37] Subsequently, a 0.1 M $CuSO_4$ solution was introduced into the GO dispersion to achieve a 5 vol% Cu loading under continuous stirring. The Cu^{2+} ions are electrostatically attracted to the negatively charged oxygen-containing groups on the GO surface, effectively anchoring them and preventing pre-mature aggregation.[37] This step ensures a uniform distribution of Cu^{2+}
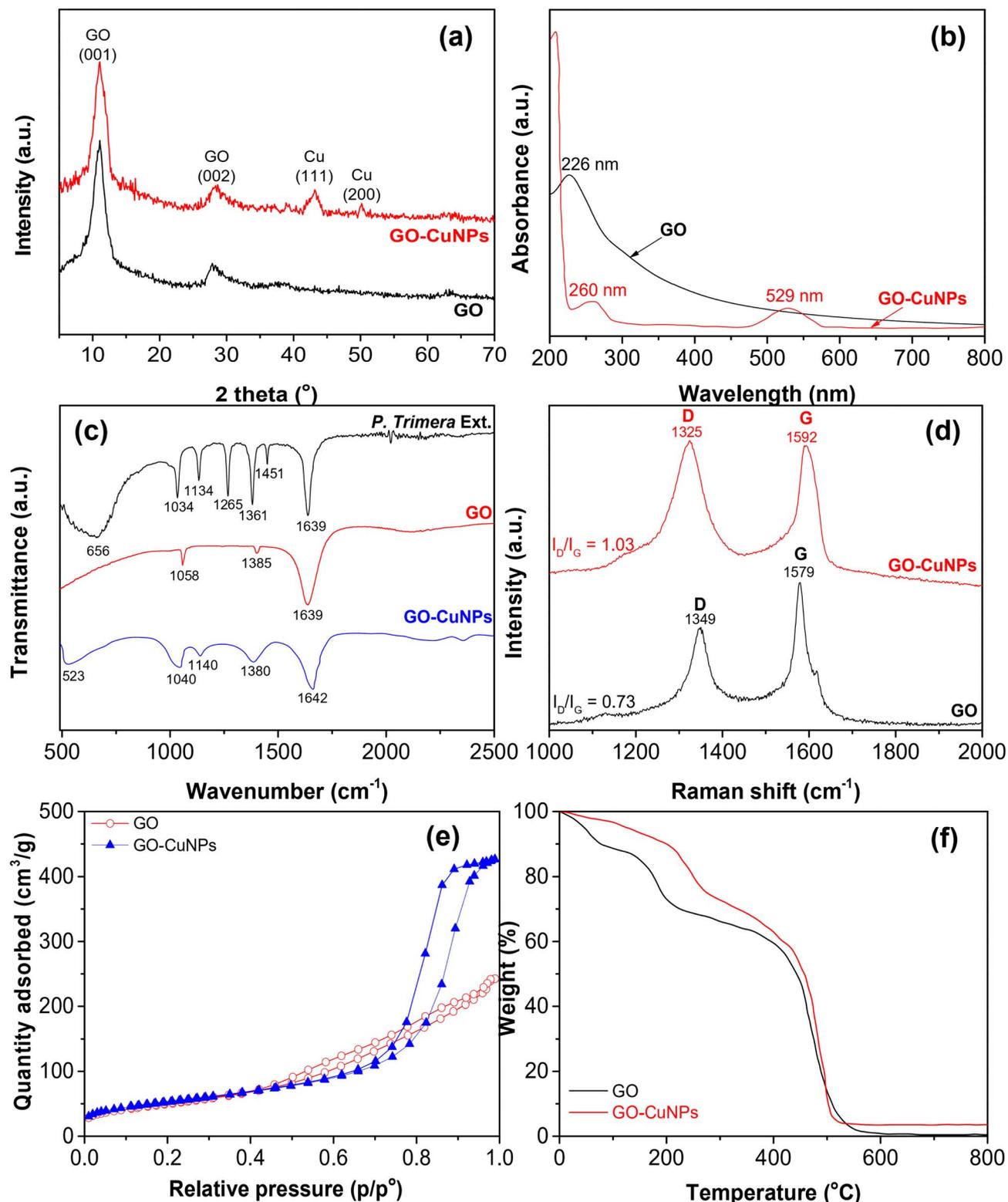
Fig. 5 (a) XRD patterns, (b) UV-vis spectra, (c) FTIR spectra, (d) Raman spectra (e) N_2 adsorption/desorption isotherms at 77 K and (f) TGA curves of GO and GO–CuNP hybrid material.

ions across the GO sheets, as evidenced by the SEM image (Fig. 3a), which shows the eventual uniform attachment of CuNPs. The reduction of Cu^{2+} to Cu^0 (metallic copper

nanoparticles, CuNPs) was facilitated by the addition of 10 mL of *P. trimera* root extract, which contains phytochemicals such as flavonoids, polyphenols, terpenoids, and alkaloids (Table

Table 1 FT-IR analysis and probable functional groups of *P. trimera* extract and GO–CuNP hybrid material

P. trimera extract wavenumber (cm^{-1})	Probable bonding	GO wavenumbers (cm^{-1})	Probable bonding	GO–CuNP hybrid material (cm^{-1})	Probable bonding
1639	C=C	1639	C=C	1642	C=C
1451	–C=O	1402	C–H	1385	C–H
1381	C–H	1058	C–O	1140	C–O–C
1265	C–N			1040	C–O
1134	C–O–C			523	Cu–O
1034	C–O				
656	C–H				

1).[38] These bioactive compounds act as both reducing and capping agents.[37] The reduction process occurred over 12 hours at room temperature under constant stirring, leading to the formation of CuNPs with an average size of 8.5 nm (Fig. 3b). The FTIR spectrum of the GO–CuNP hybrid material (Fig. 5c) exhibits a characteristic peak at 523 cm^{-1}, attributed to Cu–O stretching vibrations, indicating interactions between Cu^{2+} ions and the functional groups of the extract, such as phenols and flavonoids, which stabilize the newly formed CuNPs.[38,39] The GO sheets play a dual role in this mechanism: they act as a template for the nucleation of CuNPs and as a stabilizer to prevent their agglomeration. The oxygen-containing groups on GO not only capture Cu^{2+} ions but also facilitate the uniform deposition of CuNPs by providing anchoring sites. The UV-vis spectrum (Fig. 5b) confirms the successful synthesis of the hybrid material, displaying surface plasmon resonance peaks at 260 nm (corresponding to GO) and 529 nm (corresponding to CuNPs). Additionally, Raman spectroscopy (Fig. 5d) reveals an increase in the I_D/I_G ratio from 0.73 (GO) to 1.03 (GO–CuNP), indicating the introduction of defects and functional group interactions due to the decoration of CuNPs on the GO surface.[40] In summary, the green synthesis of the GO–CuNP hybrid material leverages the synergistic interplay between the oxygen-containing functional groups of GO and the reducing capabilities of *P. trimera* extract.[39] According to above discussion, a brief mechanistic explanation describing the green reduction

process could be proposed with three main steps as the following:[41]

• Step 1: Cu^{2+} ions coordinate to carboxyl and hydroxyl groups of GO.

• Step 2: polyphenolic compounds (flavonoids, tannins) in the neem extract donate electrons, reducing Cu^{2+} to Cu^0.

• Step 3: the catechol and carbonyl groups of plant metabolites cap the growing CuNPs, preventing aggregation.

This mechanism ensures the uniform attachment of CuNPs to GO, enhancing the stability and performance of the resulting hybrid nanofluid for photothermal applications.

3.3. Stability and thermal conductivity of nanofluids

Fig. 7a shows optical images of nanofluids containing GO–CuNP hybrid materials at varying concentrations. A noticeable color change of the nanofluids is observed as the concentration of GO–CuNP increases. Specifically, samples with higher GO–CuNP concentration exhibit a darker brown color compared to those with lower concentrations. Zeta potential measurements were performed to evaluate the colloidal stability of the nanofluids. The absolute zeta potential values for nanofluids containing 0.01%, 0.02%, 0.03%, and 0.04% GO–CuNP were recorded as 38.5 mV, 32.6 mV, 30.8 mV, and 26.2 mV, respectively (Fig. 7b–e). According to Manimaran *et al.*, hybrid nanofluids with zeta potential values exceeding 30 mV exhibit strong stability, whereas those within the range of 15–30 mV shows
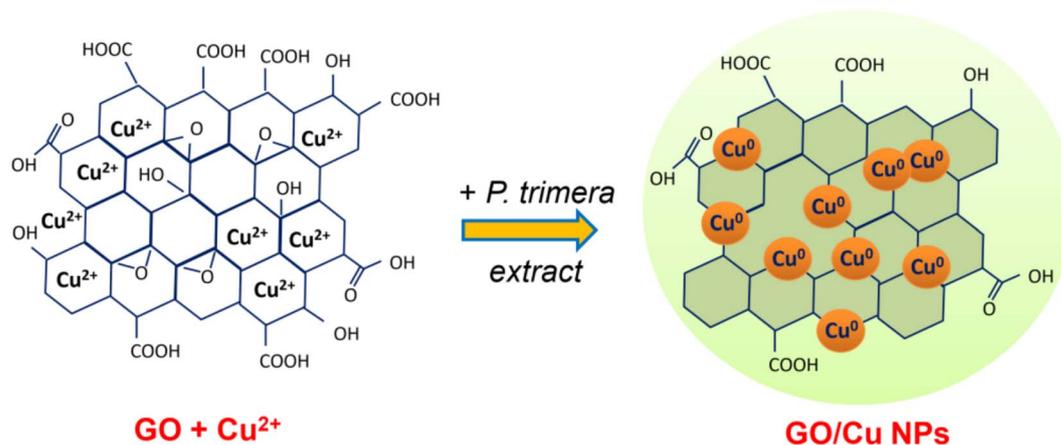

Fig. 6 The reduction mechanism of Cu^{2+} ionic to Cu^0 on the GO sheets using *P. trimera* extract.
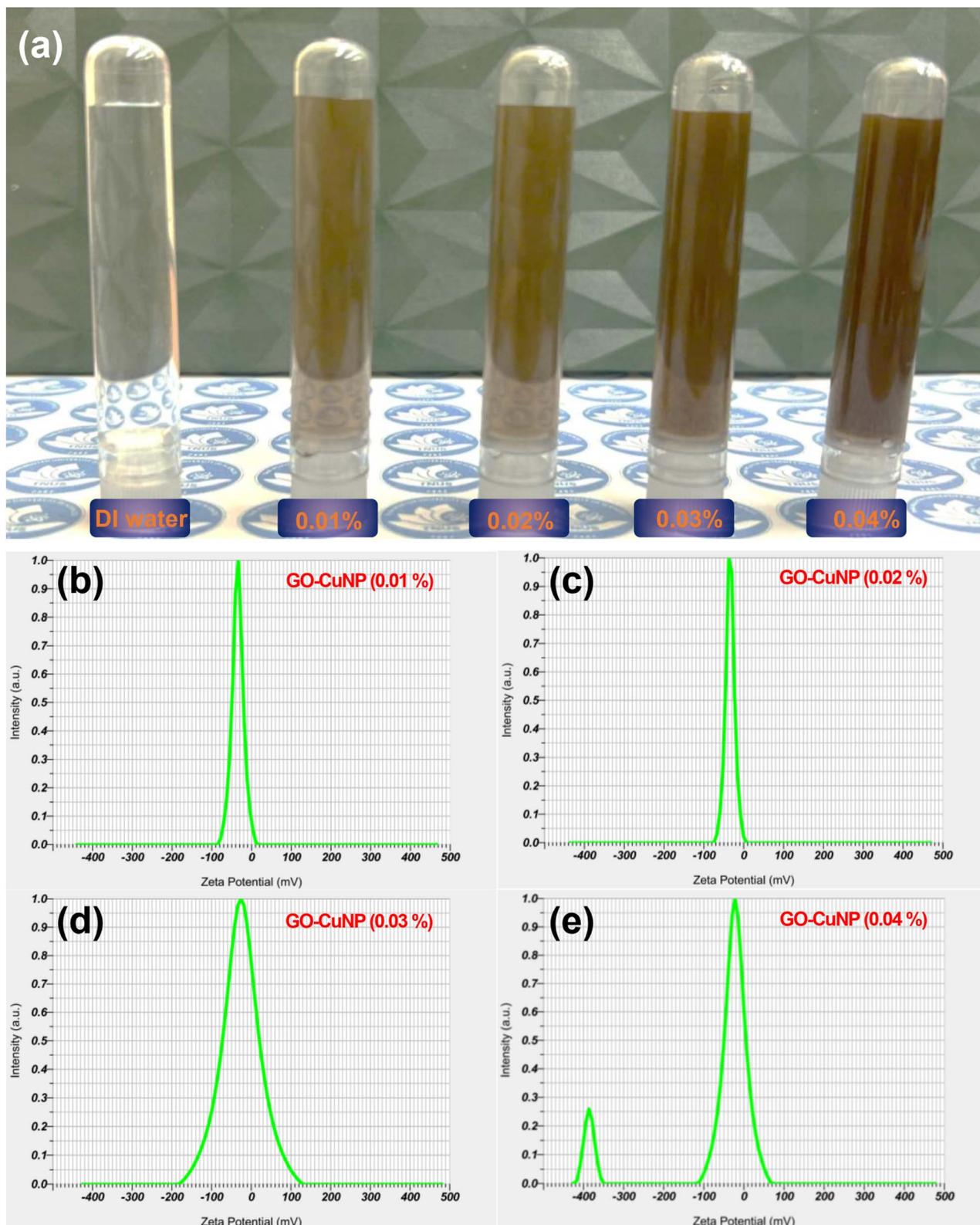
Fig. 7   (a) Optical image of nanofluids and zeta potential of nanofluids containing different GO–CuNP concentration (b) 0.01 vol%, (c) 0.02 vol%, (d) 0.03 vol% and (e) 0.04 vol%.

moderate stability.[42] Similarly, studies by Alktranee *et al.* and Wang *et al.* indicated that nanofluids require a zeta potential of approximately ±30 mV to maintain electrostatic stability; values below this threshold increase the likelihood of particle aggregation and sedimentation.[43] However, in the case of the 0.04% GO–CuNP nanofluid, two distinct peaks were observed at

−15.4 mV and −393.2 mV, suggesting the onset of nanoparticle agglomeration in the base fluid. This aggregation behavior may adversely affect the photothermal properties of the nanofluid.

Fig. 8a presents the thermal conductivity of nanofluids containing three different types of nanoadditives including CuNPs, GO, and GO–CuNPs at an identical concentration of 0.01 vol%. The results indicate that the thermal conductivity of all nanofluids is higher than that of the base fluid (water), and it further increases with temperature. Notably, a comparison of the three nanofluid systems reveals that the GO–CuNP-based nanofluid exhibits superior thermal conductivity compared with the single-component CuNP or GO nanofluids (Fig. 8b). This result is good agreement with recent studies reporting significant enhancements in the thermal conductivity of nanofluids using the hybrid nanomaterials as nanoadditives.[44–46] The thermal conductivity and thermal conductivity enhancement of nanofluids containing GO–CuNP hybrid materials with different concentrations after fabrication are shown in Fig. 8c. As observed, the thermal conductivity of nanofluids increased with the increase in the measured temperatures. This was mainly due to the improvement of Brownian motion and the reduction of agglomeration of nano

additives in nanofluids. The increase in thermal conductivity with rising temperature can be attributed to the alterations in nanoparticle aggregation and viscosity, as well as Brownian motion. These are significant factors influencing the temperature dependence of the thermal conductivity of nanofluids. As the temperature increases, it leads to: (i) reduced aggregation of nanoparticles in the liquid by reducing the surface energy of nanoparticles, (ii) improved Brownian motion by reducing viscosity, and Brownian motion acts as the main mechanism of enhancing the thermal conductivity of nanofluids.[19,47] Therefore, the thermal conductivity of nanofluids increases with increasing temperature.

As a result, the relationship between thermal conductivity of the hybrid nanofluid and base fluid (K_{nf}/K_{bf}) could be expressed by the following equation:[48]

$$\frac{K_{nf}}{K_{bf}} = A + B\varphi \qquad (2)$$

Fig. 8b shows the relationship K_{nf}/K_{bf} of the prepared nanofluid corresponding to the different measured temperatures. The obtained results indicated that the thermal
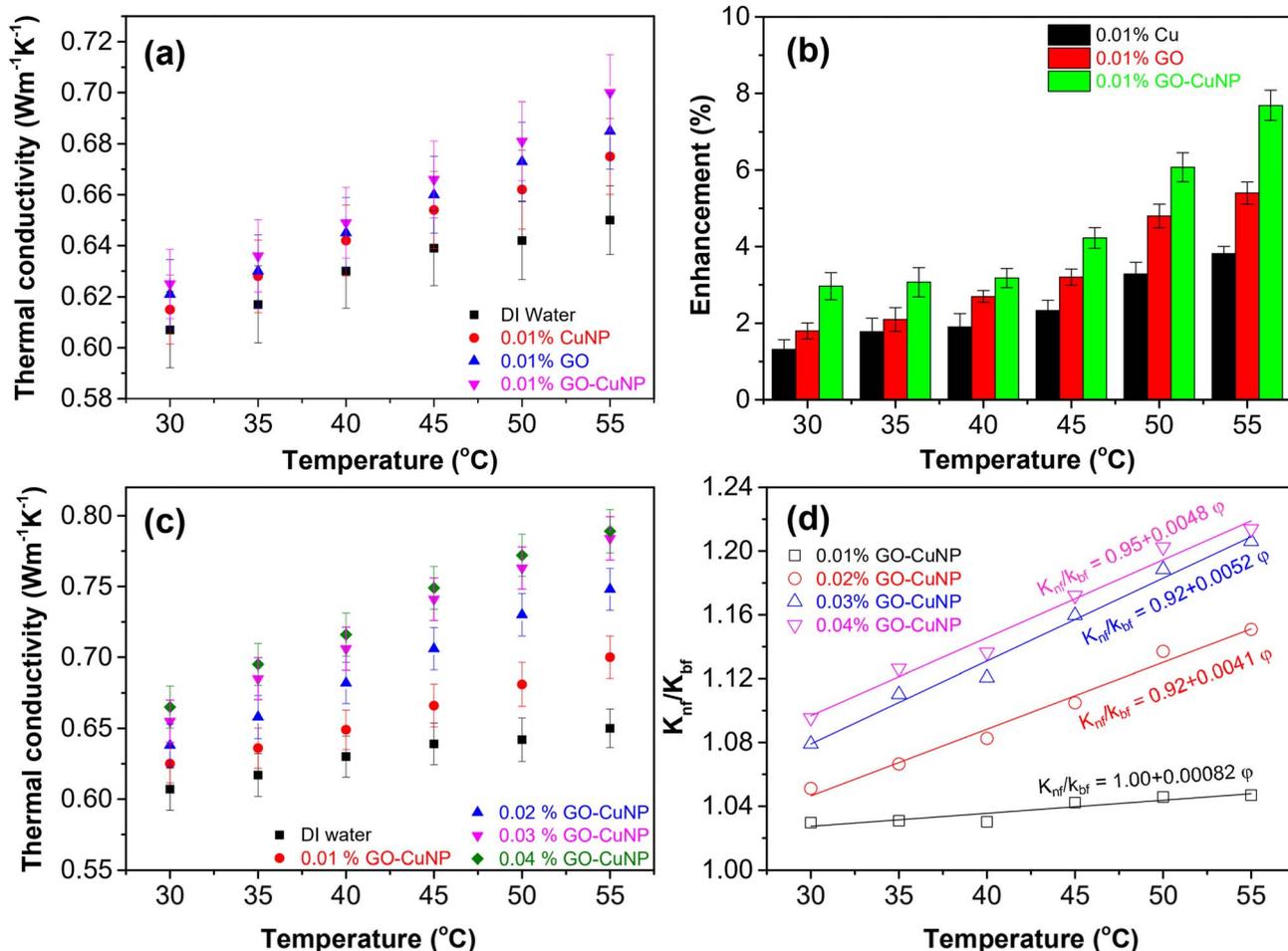

Fig. 8 (a and b) Thermal conductivity and thermal conductivity enhancement of nanofluids containing different nanoadditives; (c and d) thermal conductivity and the thermal conductivity ratio (K_{nf}/K_{bf}) of the nanofluids containing GO–Cu hybrid materials with different concentrations.

conductivity of nanofluid increase quickly at higher measured temperatures that addressed by increase of the slope of the relationship. Consequently, the improvement of the thermal conductivity of hybrid nanofluid could result from the synergistic effect of the superior properties of highly conductive materials such as graphene and CuNPs. Moreover, the incorporation of CuNPs will not only inhibit the aggregation of graphene sheets but also enhance the overall surface area of the nanofluid, hence augmenting its thermal conductivity.

To assess the thermal conductivity of nanofluids, various theoretical models can be used to predict their behavior and compare it with experimental data. In this study, the Maxwell and Hamilton–Crosser models were adopted to estimate the thermal conductivity ratio between the nanofluid and the base fluid (K_{nf}/K_{bf}). These models are expressed as follows:

Maxwell–Garnett model:[23]

$$\frac{K_{nf}}{K_{bf}} = \frac{K_{hm} + 2K_{bf} + 2\varphi(K_{hm} - K_{bf})}{K_{hm} + 2K_{bf} - \varphi(K_{hm} - K_{bf})} \tag{3}$$

Hamilton–Crosser model[49]

$$\frac{K_{nf}}{K_{bf}} = \frac{K_{hm} + (n-1)K_{bf} - (n-1)\varphi(K_{bf} - K_{hm})}{K_{hm} + (n-1)K_{bf} + \varphi(K_{bf} - K_{hm})} \tag{4}$$

In these equations, K_{nf}, K_{hm}, and K_{bf} denote the thermal conductivities of the nanofluid, the GO–Cu hybrid material and the base fluid, respectively. The parameter φ represents the volume fraction of the hybrid filler, while n ($=6$) is the empirical shape factor associated with flake-like structures.[49] The thermal conductivity of the GO–Cu hybrid was estimated using the rule-of-mixture model, expressed as:[50]

$$K_{hm} = \varphi_{GO}K_{GO} + \varphi_{Cu}K_{Cu} \tag{5}$$

where φ_{GO} and φ_{Cu} correspond to the volume fractions of GO and Cu, respectively and which are determined by EDS analysis as discussed in the previous section. The K_{GO} (≈ 2000 W m^{-1} K^{-1})[51] and K_{Cu} (≈ 401 W m^{-1} K^{-1}) are thermal conductivities of graphene and Cu. Based on eqn (5), the thermal conductivity of the GO–Cu hybrid material is calculated to be approximately 1988 W m^{-1} K^{-1}. Substituting this value into eqn (2) and (3), the thermal conductivity ratio of the nanofluid is determined and presented in Fig. 9. As observed, the values predicted by Maxwell–Garnett and Hamilton–Crosser models are considerably higher than the experimental results. This deviation can be attributed to the inherent limitations of these classical models, which primarily account for basic parameters such as the intrinsic thermal conductivity and volume fraction of the constituent materials. In practice, however, the thermal conductivity of nanofluids is influenced by a broader range of factors that are not captured in these simplified approaches. These include particle morphology, aspect ratio, surface functionalization and nanoparticle clustering. The omission of these parameters leads to an overestimation of the effective thermal conductivity when using traditional models. In addition, the interfacial resistance between the nanoparticles and the base fluid significantly influences the overall thermal
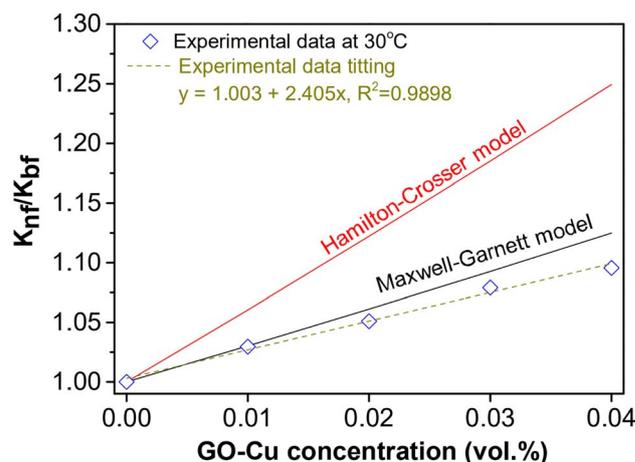

Fig. 9 Comparison of thermal conductivity ratio (K_{nf}/K_{bf}) with the calculated values predicted by Hamilton–Crosser and Maxwell–Garnett models.

conductivity of the nanofluid. Variations in thermal conductivity observed at elevated temperatures may be attributed to changes in the interfacial thermal resistance (R_K) between GO–CuNP hybrid material and the base fluid. However, direct experimental determination of the R_K remains highly challenging. Several theoretical models have accounted for the contribution of R_K to the effective thermal conductivity of nanofluids. Therefore, based on experimental data, it is possible to indirectly estimate the values of R_K. In this study, the theoretical model proposed by Chu[52] is employed to evaluate R_K. The Chu's model is defined by eqn (6):[52]

$$K_{nf} = K_{bf}\left(\frac{3 + \dfrac{2\eta^2\varphi}{\left[K_{bf}\left(\dfrac{2R_K}{L} + 13.4\sqrt{t}\right)\right]}}{3 - \eta\varphi}\right) \tag{6}$$

where L and t represent the average length and thickness of the nanomaterials. Considering that the CuNPs with relatively small and were attached to the surface of the GO sheets, the values of L and t used in eqn (6) correspond to those of GO, with $L = 1$ μm and $t = 2$ nm (Fig S1-SI). φ is the volume fraction of GO–CuNP hybrid materials in the nanofluid. The flatness ratio (η) is assumed to be 0.83, similar to that used for few-layer graphene sheets.[52] Fig. 10 presents a comparison between the calculated values of K_{nf}/K_{bf} using the Chu model and the experimental data at various temperatures to assess the accuracy and reliability of the model. The obtained results indicate that the R_K tends to decrease with increasing temperature. This trend could be attributed to the enhanced phonon vibrations within the GO–CuNP structure at elevated temperatures. The enhancement of the phonon vibrations promotes better thermal transport across the interface between GO–CuNPs and water, thereby reducing the interfacial thermal resistance. This reduction in the R_K provides an explanation for the observed increase in the thermal conductivity of nanofluid at higher
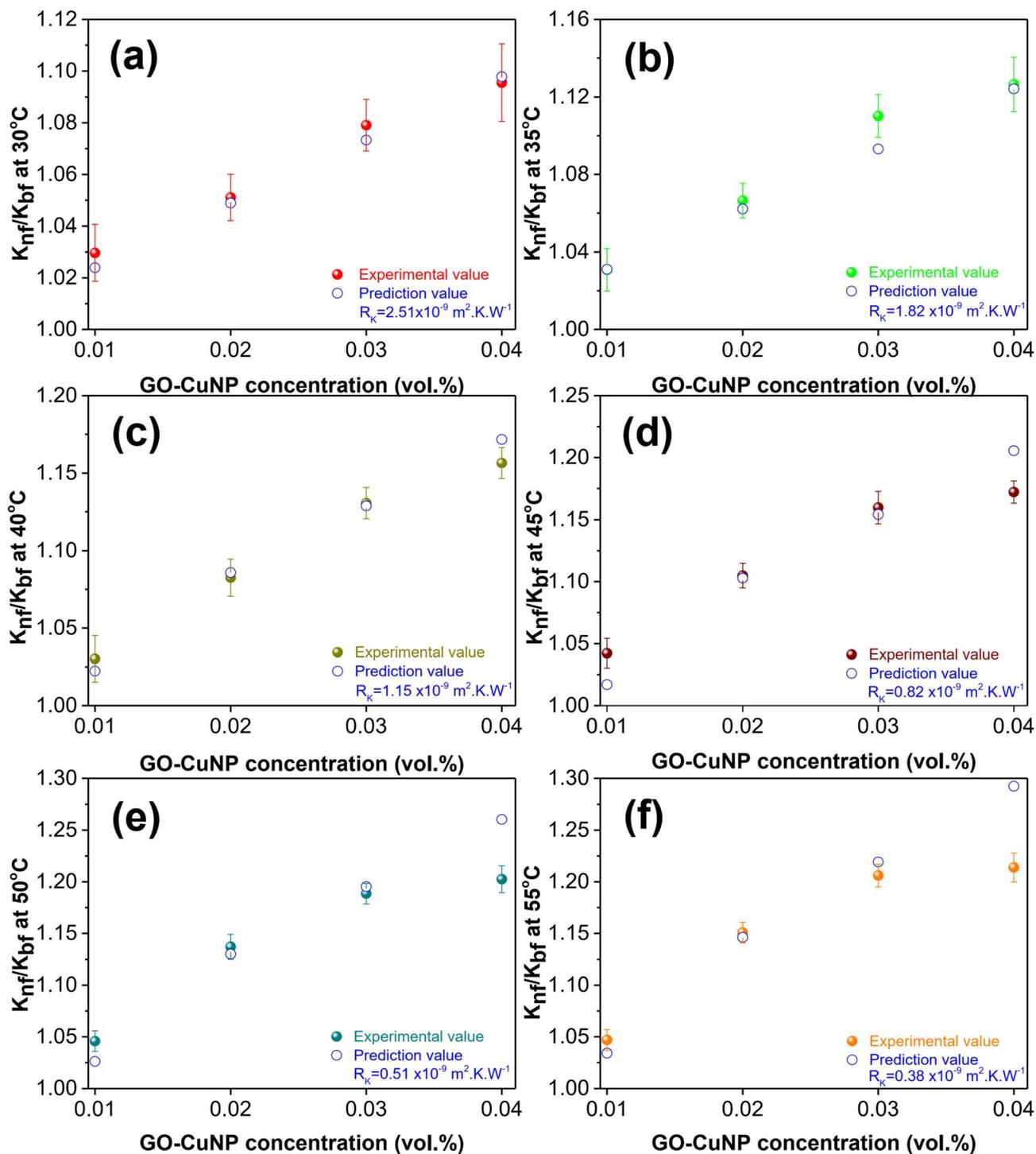
Fig. 10 Comparison of experimental value and predicted value of K_{nf}/K_{bf} at different measured temperatures (a) 30 °C, (b) 35 °C, (c) 40 °C, (d) 45 °C, (e) 50 °C and (f) 55 °C.

temperatures. Notably, for the nanofluid containing 0.04% GO–CuNP hybrid material, the predicted values at temperatures above 45 °C are significantly higher than the corresponding experimental values. This discrepancy may be explained by the agglomeration or poor stability of nanofluid with 0.04% GO–CuNP at higher concentrations, as indicated in Fig. 7. Such agglomeration increases the R_K in the nanofluid, which in turn diminishes the enhancement of the thermal conductivity and resulted in the difference between experimental and theoretical predictions.

3.4. Photothermal performance of nanofluids

The optical properties of nanofluids, including transmittance, extinction coefficient, and absorbance, provide critical insights

into their light-harvesting capabilities. Fig. 11a presents the spectral transmittance of DI water and nanofluids containing different nanoadditives. At the same concentration, the GO nanofluid exhibits higher transmittance than those containing CuNPs or GO–CuNP hybrid materials, reflecting the inherently higher transparency of GO. In contrast, the presence of CuNPs in the GO–CuNP hybrid msterial acts as light-scattering centers, reducing transmittance relative to GO. Furthermore, increasing the GO–CuNP concentration from 0.01 to 0.04 vol% leads to a progressive decrease in transmittance across the 200–1350 nm

Fig. 11 (a) Transmittances, (b) extinction coefficients and (c) absorbance of DI water and the prepared nanofluid.

wavelength range, consistent with predictions from Mie scattering theory.[53] For instance, the average transmittance of the 0.01 vol% GO–CuNP nanofluid in the 200–880 nm range is reduced by over 25% compared to water, while for 0.04 vol% GO–CuNPs, it decreases to approximately 40%, indicating stronger light absorption at higher nanoparticle loadings. The spectral extinction coefficients shown in Fig. 11b further supports this trend. The extinction coefficient increases with GO–CuNP content, mirroring the reduction in transmittance. This behavior aligns with previous reports by Lee and Jiang,[54] as the extinction coefficient is linearly dependent on nanoparticle concentration and inversely related to the optical path length. Consequently, sufficient nanoparticle loading allows complete absorption of incident light over a specific optical path. Fig. 11c presents the absorption characteristics of nanofluids with varying nanoparticle types and concentrations. The results indicate that nanofluids with higher nanoparticle content achieve stronger light absorption, demonstrating that hybrid GO–CuNP nanofluids outperform single-component systems in capturing incident light. These superior optical properties suggest that nanofluids containing hybrid nanoparticles are highly promising candidates for efficient solar-absorbing fluids in applications such as solar thermal energy harvesting.

The photothermal conversion efficiency of nanofluids containing GO–CuNP hybrid material significantly depends on the temperature change of the nanofluids as a function of illumination time. Fig. 12a illustrates the temperature profiles of fluids containing different types of nanoparticles during an irradiation period of 0 to 60 minutes. The results show that the nanofluids consistently exhibit higher temperatures than pure water at all time points. Among the nanofluids, the GO–Cu hybrid nanofluid, which possesses higher thermal conductivity, reaches higher temperatures compared with those containing only GO or CuNPs. This enhanced temperature rise is closely associated with the improved photothermal conversion efficiency of the nanofluids.

The following formula is used to evaluate the photothermal conversion efficiency (PTE) of nanofluids containing GO–CuNP hybrid materials:[55,56]

$$\text{PTE} = \frac{m_{nf}c_{nf}(T_s - T_i)}{GA\Delta t} \tag{7}$$

where m_{nf} is the mass of the nanofluid, c_{nf} is the specific heat of the nanofluid. The specific heat of nanofluids could be estimated by using the mixture theory expressed as the following eqn (8):[57]

$$c_{nf} = (1 - \varphi)c_w + \varphi c_{hm} \tag{8}$$

where c_w and c_{hm} is the specific heat of water (≈ 4.18 kJ $°C^{-1}$) and GO–Cu hybrid material. The specific heat of GO–Cu hybrid material could be calculated by using the eqn (7) and the composition of GO–Cu hybrid material determined by EDS. The c_{nf} values were estimated to be 4.142 kJ $°C^{-1}$, 4.145 kJ $°C^{-1}$, 4.143 kJ $°C^{-1}$, 4.107 kJ $°C^{-1}$, 4.071 kJ $°C^{-1}$ and 4.038 kJ $°C^{-1}$ for nanofluid containing CuNPs (0.01 vol%), GO (0.01 vol%), GO–CuNP (0.01 vol%), GO–CuNP (0.02 vol%), GO–CuNP (0.03 vol%)

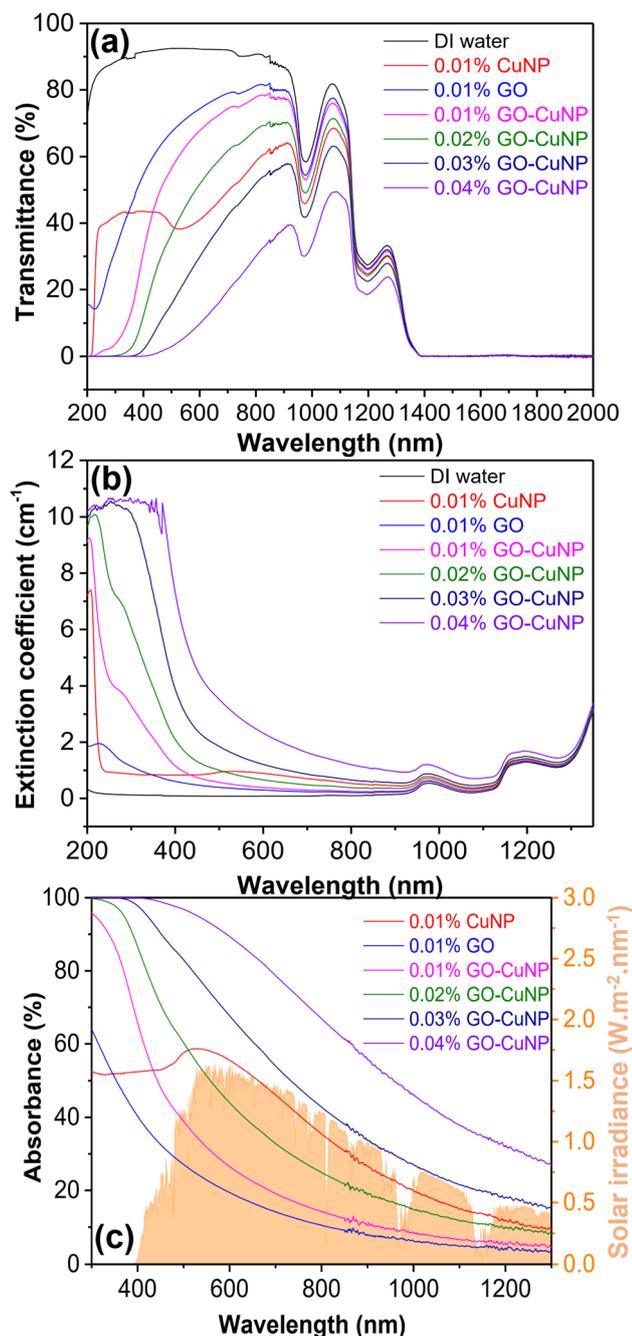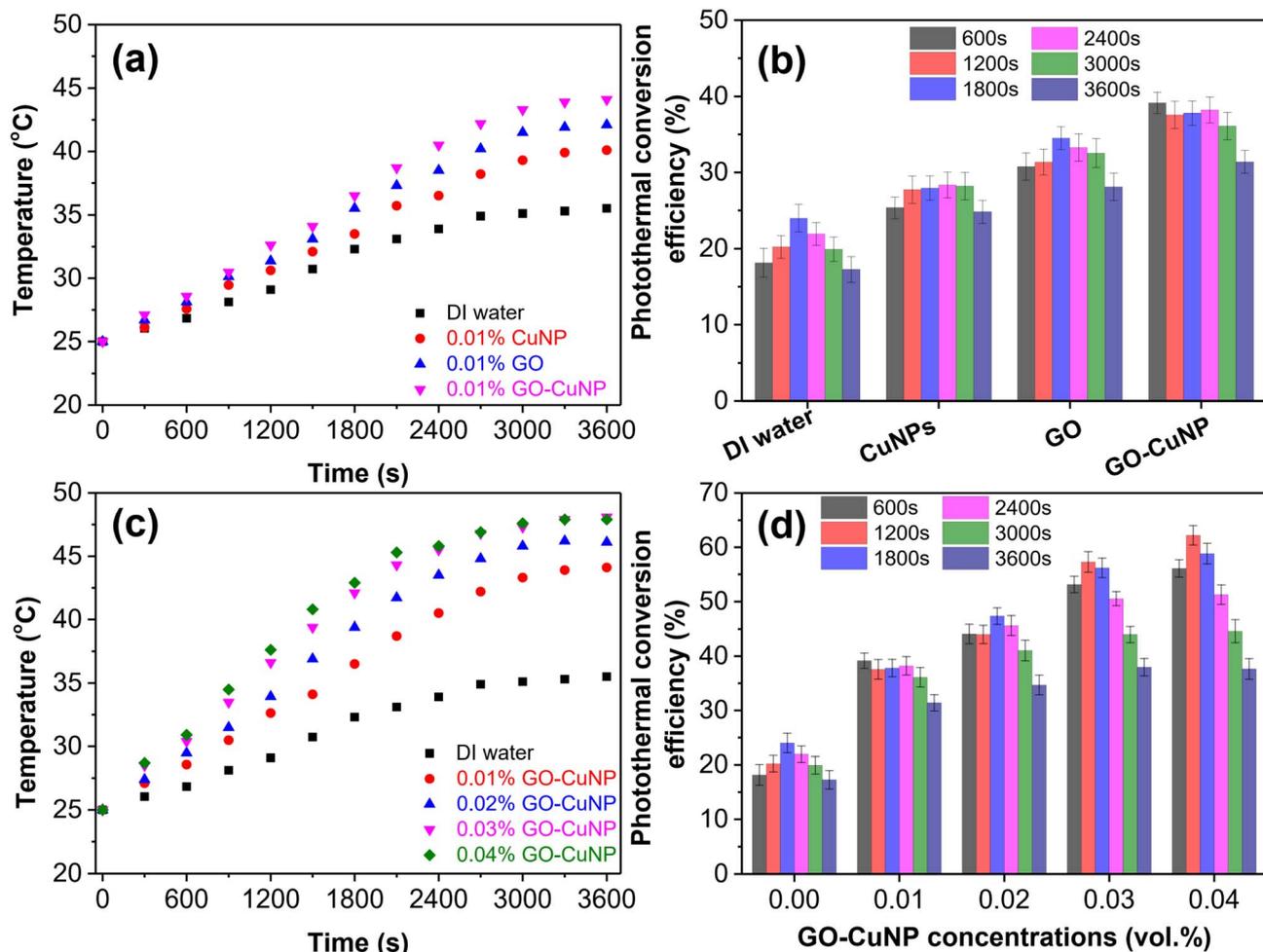Fig. 12 The temperature profiles and the photothermal conversion efficiency of (a and b) nanofluids containing different nanoadditives and (c and d) nanofluids containing GO–Cu hybrid materials with different concentrations.

and GO–CuNP (0.04 vol%), respectively. T_s and T_i are the starting and ending temperatures, respectively, G is the solar irradiation (1000 Wm^{-2}), A is the surface area of the irradiated liquid, and Δt is the illumination time, here the first 10 min was chosen for the calculation to prevent the effects of heat loss at high temperatures. Fig. 12b shows the photothermal conversion efficiency calculated by using eqn (7) of nanofluids containing GO–CuNP hybrid materials. The photothermal conversion efficiency of water was determined to be 18%. Fig. 12b presents the PTE calculated using eqn (6) of DI water and the nanofluids containing CuNPs, GO and GO–CuNP hybrid material with a concentration of 0.01 vol%. It can be observed that the nanofluid containing GO–Cu hybrid material exhibits higher PTE values compared with those containing only GO or Cu, which is consistent with the thermal conductivity measurements of the nanofluids. The highest PTE value for the GO–Cu nanofluid at a concentration of 0.01 vol% occurs at approximately 600 s, after which the efficiency decreases. This decline is primarily attributed to increased heat loss resulting from the rising nanofluid temperature. In practice, heat loss occurs through convection to the surrounding

environment and thermal radiation from the upper surface, both of which are directly related to the nanofluid temperature.[58,59] For example, the PTE of the 0.01 vol% GO–Cu nanofluid decreases from 38% to 31% as the irradiation time increases from 600 s to 3600 s. When compared with nanofluids containing only GO or CuNPs, the GO–CuNP nanofluid consistently exhibits higher PTE values across all irradiation periods. These results demonstrate that nanofluids incorporating hybrid materials possess superior PTE performance compared with those containing single-component nanoparticles.

The effect of GO–CuNP concentration on both the temperature profile and the photothermal energy (PTE) of the nanofluid is presented in Fig. 12c and d. It is clear that a profound improvement in the photothermal conversion properties of water was achieved after the addition of GO–CuNP hybrid materials. The temperature of the nanofluids increased faster than that of water during an illumination period of 1 h. For example, the highest temperature of the nanofluids containing 0.03% GO–CuNP hybrid materials was measured to be 48.1 °C, which increased about 37% compared to the temperature of

water (35.2 °C). In addition, the temperature of the nanofluid containing the GO–CuNP hybrid material increase with the increase of the concentration. The obtained results indicated that increasing the concentration of GO–CuNP leads to higher PTE values. The highest PTE was obtained to be 62% with the nanofluid containing 0.04 vol% GO–CuNP after 20 min illumination which is three time higher than that of DI water. This result is explained by the enhanced thermal conductivity of the nanofluids and the increased absorption of the nanofluid with the addition of GO–CuNP hybrid materials. These results suggest that the concentration of hybrid nanoparticles plays a critical role in optimizing the thermal and photothermal performance of the nanofluid, likely due to increased light absorption and more efficient heat transfer at higher nanoparticle loadings. Furthermore, it can be observed that increasing the GO–CuNP concentration from 0 to 0.04 vol% initially leads to an increase in PTE, reaching a maximum value, after which it gradually decreases. This behavior can be explained as follows: increasing the GO–CuNP concentration enhances the absorption coefficient of the nanofluid, thereby improving its optical absorption capability. At a certain concentration, the incident solar radiation can be almost completely absorbed; however, beyond the concentration corresponding to the maximum temperature, the effective radiation penetration within the fluid is reduced. The enhanced energy absorption raises the surface temperature of the nanofluid, which in turn increases heat loss to the surrounding environment. This increase in thermal dissipation ultimately reduces the PTE of the nanofluid under prolonged irradiation. Compared with nanofluids containing only GO or CuNPs, the GO–CuNP hybrid nanofluid consistently demonstrates higher PTE across all concentrations and irradiation periods, highlighting the advantage of hybrid nanoparticles in enhancing both optical absorption and photothermal conversion efficiency. These results are consistent with previous studies on the photothermal conversion efficiency of reported nanofluids (Table 2), which typically report PTE $\approx$ 40–60% under similar conditions. Exceptional values, such as PTE = 82.64% for rGO/N-CQD nanofluids, arise from strong optical absorption and electronic coupling, while evaporation-based solar-steam systems show higher apparent efficiencies due to latent heat contributions and interfacial heat localization.[60] The obtained results were in lined with the experimentally validated range, confirming their reliability and reproducibility. These results confirm that combining different nanomaterials in a single fluid can significantly improve the overall performance of nanofluids for solar energy applications.

4. Conclusions

GO–CuNP hybrid materials were successfully synthesized *via* a green method using *P. trimera* extract, producing uniformly distributed Cu nanoparticles (~8.5–10.7 nm) anchored on GO sheets. The hybrid formation was confirmed, revealing strong interactions between CuNPs and GO functional groups. Nanofluids containing GO–CuNPs exhibited superior thermal conductivity compared with single-component nanofluids (GO

Table 2 Photothermal conversion efficiency of the reported nanofluids

Ref.	Nanoadditives	Base fluid	Concentration	PTE
Behura et al.[61]	Al_2O_3	Water	10–100 ppm	39%
Li et al.[62]	Single layer Gr	Water	0–100 ppm	46%
	GO	Water	0–100 ppm	49%
Sattar et al.[63]	GO	Water	0.02–0.03 wt%	42%
Chen et al.[64]	GO	Water	0.02–0.1 wt%	97%
Sattar et al.[5]	GO–ZnO	Water	0.02–0.03 wt%	64%
	GO–FeO	Water	0.02–0.03 wt%	58%
Wang et al.[65]	Fe_2O_3-GO	Water	0.001–0.007 wt%	57%
Tong et al.[66]	Fe_3O_4-MWCNTs	Water	0.01 wt%	60%
Javidi et al.[60]	rGO/NQD	Water	0.01–0.1 vol%	82%
Qu et al.[67]	GO	Water	10–180 ppm	28%
This work	GO–CuNP	Water	0–0.04 vol%	62%

or CuNP) and water, with enhancement increasing with temperature. Optical properties of the nanofluids demonstrated that increasing the GO–CuNP concentration reduced transmittance and increased extinction and absorption coefficients, enhancing light-harvesting capacity. Photothermal measurements confirmed that GO–CuNP nanofluids consistently reached higher temperatures and PTE values compared with GO or CuNP nanofluids. The maximum PTE of 62% was obtained at 0.04 vol% GO–CuNPs, approximately three times higher than that of DI water. The synergistic combination of GO and CuNPs in a hybrid nanofluid improves thermal conductivity, optical absorption, and photothermal conversion efficiency, demonstrating their strong potential as efficient solar-absorbing fluids for solar thermal energy applications.

Conflicts of interest

The authors declare no possible conflict of interests.

Data availability

The authors confirm that the data supporting the findings of this study are available within the articles. Raw data that support the findings of this study are available from the corresponding author, upon reasonable request.

Supplementary information (SI) is available. See DOI: https://doi.org/10.1039/d5ra03959b.

Acknowledgements

References

1 B. Singh and S. Sood, *Hybrid Adv.*, 2024, **6**, 100192.
2 V. B. Mbayachi, E. Ndayiragije, T. Sammani, S. Taj, E. R. Mbuta and A. ullah khan, *Results Chem.*, 2021, **3**, 100163.
3 Z. Su, N. Zhao, X. Li, J. Liu and L. Yang, *Int. J. Heat Mass Transfer*, 2025, **241**, 126702.

4 H. Nikpourian and A. Allahbakhsh, *Chem. Eng. J.*, 2025, **512**, 162457.

5 A. Sattar, B. Bofeng, M. Adeel Munir, M. Farooq, S. Bilal, M. I. Khan, N. S. Akbar, M. I. Khan, M. Rehan and F. Riaz, *Energy Convers. Manage.:X*, 2025, **26**, 100898.

6 H. Su and Y. H. Hu, *Chem. Commun.*, 2023, **59**, 6660–6673.

7 L. Zhang, L. Chen, J. Liu, X. Fang and Z. Zhang, *Renew. Energy*, 2016, **99**, 888–897.

8 M. Vakili, S. M. Hosseinalipour, S. Delfani and S. Khosrojerdi, *Sol. Energy Mater. Sol. Cells*, 2016, **152**, 187–191.

9 S. Khosrojerdi, A. M. Lavasani and M. Vakili, *Sol. Energy Mater. Sol. Cells*, 2017, **164**, 32–39.

10 L. Chen, C. Xu, J. Liu, X. Fang and Z. Zhang, *Sol. Energy*, 2017, **148**, 17–24.

11 J. Sarkar, P. Ghosh and A. Adil, *Renewable Sustainable Energy Rev.*, 2015, **43**, 164–177.

12 M. Mehrali, M. K. Ghatkesar and R. Pecnik, *Appl. Energy*, 2018, **224**, 103–115.

13 A. Vărdaru, G. Huminic, A. Huminic, C. Fleacă, F. Dumitrache and I. Morjan, *Diamond Relat. Mater.*, 2023, **132**, 109688.

14 Z. Zeng, L. Lu, X. Cao, T. Xie, X. Lu, L. Zhou, J. Cheng, L. Ma and D. Jing, *J. Colloid Interface Sci.*, 2025, **682**, 502–518.

15 G. Huminic, A. Vărdaru, A. Huminic, C. Fleacă and F. Dumitrache, *J. Mol. Liq.*, 2024, **408**, 125347.

16 C. Campos, D. Vasco, C. Angulo, P. A. Burdiles, J. Cardemil and H. Palza, *Energy Convers. Manage.*, 2019, **181**, 247–257.

17 W. Yu and H. Xie, *J. Nanomater.*, 2012, **2012**, 435873.

18 J. A. Eastman, S. U. S. Choi, S. Li, W. Yu and L. J. Thompson, *Appl. Phys. Lett.*, 2001, **78**, 718–720.

19 P. Van Trinh, N. N. Anh, B. H. Thang, L. D. Quang, N. T. Hong, N. M. Hong, P. H. Khoi, P. N. Minh and P. N. Hong, *RSC Adv.*, 2016, **7**, 318–326.

20 S. Veeramachaneni, S. K. Pisipaty, D. R. Vedula, A. B. Solomon and V. S. Harsha, *J. Therm. Anal. Calorim.*, 2022, **147**, 5985–5999.

21 F. Bonaccorso, L. Colombo, G. Yu, M. Stoller, V. Tozzini, A. C. Ferrari, R. S. Ruoff and V. Pellegrini, *Science*, 2015, **347**(6217), 1246501.

22 A. H. Shaik, S. Chakraborty, S. Saboor, K. R. Kumar, A. Majumdar, M. Rizwan, M. Arıcı and M. R. Chandan, *J. Therm. Anal. Calorim.*, 2024, **149**(7), 2953–2968.

23 P. Van Trinh, N. N. Anh, B. H. Thang, L. D. Quang, N. T. Hong, N. M. Hong, P. H. Khoi, P. N. Minh and P. N. Hong, *RSC Adv.*, 2016, **7**, 318–326.

24 S. H. A. Ahmad, R. Saidur, I. M. Mahbubul and F. A. Al-Sulaiman, *Renewable Sustainable Energy Rev.*, 2017, **73**, 1014–1030.

25 V. K. Pustovalov and L. G. Astafyeva, *Nanotechnol. Environ. Eng.*, 2018, **3**(1), 15.

26 I. J. Lithi, K. I. Ahmed Nakib, A. M. S. Chowdhury and M. Sahadat Hossain, *Nanoscale Adv.*, 2025, **7**, 2446–2473.

27 N. Van Hao, D. H. Tung, T. T. Thao, V. X. Hoa, N. H. Thoan, P. T. Tan, P. N. Minh, J. Fal, G. Żyła and P. Van Trinh, *J. Therm. Anal. Calorim.*, 2023, **148**(15), 7579–7590.

28 N. A. Nguyen, V. H. Nguyen, V. N. Pham, T. T. Le, V. T. Nguyen and V. T. Pham, *Adv. Nat. Sci.:Nanosci. Nanotechnol.*, 2021, **12**, 035009.

29 T. Guo, C. Bulin, Z. Ma, B. Li, Y. Zhang, B. Zhang, R. Xing and X. Ge, *ACS Omega*, 2021, **6**(25), 16535–16545.

30 W. Dou, J. Liu and M. Li, *J. Mol. Liq.*, 2021, **322**, 114516.

31 L. Zhao, J. Chen, N. Xiong, Y. Bai, A. Yilihamu, Q. Ma, S. Yang, D. Wu and S. T. Yang, *Sci. Total Environ.*, 2019, **682**, 591–600.

32 A. L. Patterson, *Phys. Rev.*, 1939, **56**, 978.

33 N. Van Hao, D. H. Tung, T. T. Thao, V. X. Hoa, N. H. Thoan, P. T. Tan, P. N. Minh, J. Fal, G. Żyła and P. Van Trinh, *J. Therm. Anal. Calorim.*, 2023, **148**, 7579–7590.

34 Z. Alhalili, *Arabian J. Chem.*, 2022, **15**, 103739.

35 W. W. Andualem, F. K. Sabir, E. T. Mohammed, H. H. Belay and B. A. Gonfa, *J. Nanotechnol.*, 2020, **2020**, 2932434.

36 D. M. Nzilu, E. S. Madivoli, D. S. Makhanu, S. I. Wanakai, G. K. Kiprono and P. G. Kareru, *Sci. Rep.*, 2023, **13**(1), 1–18.

37 S. Ahmed, M. Ahmad, B. L. Swami and S. Ikram, *J. Adv. Res.*, 2016, **7**, 17–28.

38 K. O. Nguyen Thi, T. H. Le, H. D. Nguyen, Q. H. Nguyen, T. Y. Do, T. P. N. Mai and T. V. A. Le, *J. Essent. Oil Bear. Plants*, 2022, **25**, 273–281.

39 V. T. Nguyen, J. A. Sakoff and C. J. Scarlett, *Chem. Biodiversity*, 2017, **14**, e1600396.

40 A. C. Ferrari and D. M. Basko, *Nat. Nanotechnol.*, 2013, **8**(4), 235–246.

41 M. K. Ghosh, S. Sahu, I. Gupta and T. K. Ghorai, *RSC Adv.*, 2020, **10**, 22027–22035.

42 M. Manimaran, M. N. Norizan, M. H. M. Kassim, M. R. Adam, N. Abdullah and M. N. F. Norrrahim, *RSC Adv.*, 2025, **15**, 14088–14125.

43 M. Alktranee and P. Bencs, *Int. Rev. Appl. Sci. Eng.*, 2023, **14**, 241–255.

44 R. Pourrajab, M. Behbahani and R. Mansouri, *J. Therm. Anal. Calorim.*, 2025, **150**(10), 8015–8027.

45 M. Hemmat Esfe, D. Toghraie and M. Sarbaz Karajabad, *J. Therm. Anal. Calorim.*, 2025, **150**(12), 9255–9264.

46 M. Manimaran, M. N. Norizan, M. H. M. Kassim, M. R. Adam, N. Abdullah and M. N. F. Norrrahim, *RSC Adv.*, 2025, **15**, 14088–14125.

47 S. P. Jang and S. U. S. Choi, *Appl. Phys. Lett.*, 2004, **84**, 4316–4318.

48 N. Van Hao, D. H. Tung, T. T. Thao, V. X. Hoa, N. H. Thoan, P. T. Tan, P. N. Minh, J. Fal, G. Żyła and P. Van Trinh, *J. Therm. Anal. Calorim.*, 2023, **148**(15), 7579–7590.

49 R. L. Hamilton and O. K. Crosser, *Ind. Eng. Chem. Fundam.*, 2002, **1**, 187–191.

50 M. P. Beck, Y. Yuan, P. Warrier and A. S. Teja, *J. Appl. Phys.*, 2010, **107**, 066101.

51 A. A. Balandin, *Nat. Mater.*, 2011, **10**, 569–581.

52 K. Chu, W. S. Li and F. L. Tang, *Phys. Lett. A*, 2013, **377**, 910–914.

53 C. F. Bohren and D. R. Huffman, *Absorption and Scattering of Light by Small Particles*, John Wiley & Sons, Hoboken, NJ, 2008.

54 S. H. Lee and S. P. Jang, *Int. J. Heat Mass Transfer*, 2013, **67**, 930–935.

55 R. Zhang, J. Qu, M. Tian, X. Han and Q. Wang, *Int. J. Energy Res.*, 2018, **42**, 2456–2464.

56 Y. Bao, Q. Luo, X. Zheng and G. Qin, *Diamond Relat. Mater.*, 2023, **140**, 110489.

57 B. C. Pak and Y. I. Cho, *Exp. Heat Transf.*, 1998, **11**, 151–170.

58 M. Chen, Y. He, J. Zhu and D. Wen, *Appl. Energy*, 2016, **181**, 65–74.

59 J. Qu, M. Tian, X. Han, R. Zhang and Q. Wang, *Appl. Therm. Eng.*, 2017, **124**, 486–493.

60 M. Javidi and M. H. Entezari, *ACS Appl. Energy Mater.*, 2025, **8**, 8442–8457.

61 A. K. Behura and H. K. Gupta, *Mater. Today: Proc.*, 2020, **22**, 1664–1668.

62 Z. Li, A. Kan, K. Wang, Y. He, N. Zheng and W. Yu, *Appl. Therm. Eng.*, 2022, **203**, 117948.

63 A. Sattar, M. Farooq, M. Amjad, M. A. Saeed, S. Nawaz, M. A. Mujtaba, S. Anwar, A. M. El-Sherbeeny, M. E. M. Soudagar, E. P. Bandarra Filho, Q. Ali, M. Imran and A. Pettinau, *Energies*, 2020, **13**, 4956.

64 L. Chen, C. Xu, J. Liu, X. Fang and Z. Zhang, *Sol. Energy*, 2017, **148**, 17–24.

65 D. Wang, Y. Jia, Y. He, L. Wang, H. Xie and W. Yu, *Energy Convers. Manage.*, 2019, **199**, 111996.

66 Y. Tong, T. Boldoo, J. Ham and H. Cho, *Energy*, 2020, **196**, 117086.

67 J. Qu, L. Shang, Q. Sun, X. Han and G. Zhou, *Renewable Energy*, 2022, **195**, 516–527.